ELSEVIER

Contents lists available at ScienceDirect

International Journal of Applied Earth Observation and Geoinformation

journal homepage: www.elsevier.com/locate/jag





Cropping intensity map of China with 10 m spatial resolution from analyses of time-series Landsat-7/8 and Sentinel-2 images

Luo Liu a , Shanggui Kang a , Xiliu Xiong b , Yuanwei Qin c , Jie Wang d , Zhenjie Liu e , Xiangming Xiao $^c,^*$

- a Guangdong Province Key Laboratory for Land use and consolidation, South China Agricultural University, Guangzhou 510642, China
- b Institute of Ecological Environment Protection, Guangxi Eco-Engineering Vocational and Technical College, Guangxi 545004, China
- ^c School of Biological Sciences, Center for Earth Observation and Modeling, University of Oklahoma, Norman, OK 73019, USA
- ^d College of Grassland Science and Technology, China Agricultural University, Beijing 100083, China
- e Guangdong Provincial Key Laboratory of Urbanization and Geo-simulation, School of Geography and Planning, Sun Yat-sen University, Guangzhou 510275, China

ARTICLE INFO

Keywords: Cropping intensity Google Earth Engine Crop phenology Remote sensing Crop growth cycle

ABSTRACT

Cropping intensity maps at high spatial resolution play a crucial role in guiding agricultural policies and ensuring food security. So far, most of nationwide cropping intensity maps have been developed from satellite images at moderate or coarse resolutions. In this study, we first assembled and integrated time-series dataset with high spatial resolution, specifically Landsat-7, Landsat-8 and Sentinel-2 imagery in 2017. We then used an object- and phenology-based algorithm and integrated images to create a 10-m resolution cropping intensity map over China. The map evaluation results revealed an overall accuracy of 96.68 \pm 0.01 % and a Kappa coefficient of 0.90. In 2017, single cropping dominated the agricultural practices in China, with an approximate area of 1.189 \times 10 6 km² \pm 7.90 \times 10 3 km², constituted 79.26 % of the entire cropland area. Simultaneously, double and triple cropping covered approximately 0.306 \times 10 6 km² \pm 8.03 \times 10 3 km² and 5.00 \times 10 3 \pm 1.75 \times 10 3 km², corresponding to 20.41 % and 0.33 % of the entire cropland area, respectively. On average, the national multiple cropping index (MCI) was 1.21. The results in the study prove the reliability of the generated mapping products and high potential of the developed mapping framework (the algorithm and integrated datasets), which can be readily applied to quantify the interannual changes of cropping pattern on a nationwide level with a high spatial resolution.

1. Introduction

Cropland area, crop yield, and cropping intensity (CI, i.e., the crops cultivation frequency on a cropland parcel within a year) are important factors influencing global food security (Kogan, 2019). Since early 1980s, rapid economic and population growth has resulted in significant cropland transformation in China (Liu et al., 2005). Several strategies have been implemented to protect and conserve the croplands in China (Zhang et al., 2016; He et al., 2021b), nevertheless, cropland continues to be lost owing to urbanization and industrialization (Liu et al., 2019). The per capita cropland of China was only about 0.001 km², much lower than the global mean of 0.002 km² (He et al., 2017; FAOSTAT, 2018). Losses of labor in rural areas, driven by an influx of rural people into cities for higher-paying jobs, also reduced crop cultivation (Li et al., 2018). These factors put substantial pressure on food production in

China (Wang et al., 2018; Doelman et al., 2019; Liu et al., 2022). Moreover, in view of global food prices fluctuations led by Russia-Ukraine conflict (Lin et al., 2023), China's food import also faces great uncertainty. Greater emphasis should be placed on domestic food production efficiency. Several studies have reported that double- and triple-cropping fields increase food production by improving cropland efficiency, however, increasing cropping intensity puts more stress on the land and can reduce yields or require higher inputs (Rufin et al., 2019; Xiang et al., 2019). Given these contexts, rational planning of cropping intensity is increasingly important to ensure food production and security in China.

Accurate cropping intensity data can provide meaningful information to guide the formulation of agricultural strategies (Sun et al., 2019), and come from agricultural census statistics and remote sensing imagery (Panigrahy et al., 2005). Agricultural census data provide the cropland

E-mail address: xiangming.xiao@ou.edu (X. Xiao).

^{*} Corresponding author.

and sowing area at county scale but usually lack detailed spatial distribution information and lag in data collection (Qiu et al., 2018). Therefore, statistical investigation cannot meet the needs of governments and scientists for cropping intensity maps at high spatial resolution (Hao et al., 2019). Satellite remote sensing provides repeated observations of land surfaces, allowing the surveys of crop phenology and cropland utilization over wide areas (Li et al., 2015; Shao et al., 2016). Therefore, remote sensed images have become important data sources for rapid and large-scale data collection from multiple cropping fields (Peng et al., 2011; Wu et al., 2018). Most existing cropping intensity maps of China have been generated using MODIS images with moderate spatial resolutions (250-m and 500-m) (Yan et al., 2014; Ding et al., 2015; Yan et al., 2019). These products often show high accuracy as the temporal resolution is high, however, their spatial resolution is coarse. Each MODIS pixel often comprises several crop fields and/or crop types, which precludes accurate mapping of small fields, especially in southern China (Liu et al., 2020; Qiu et al., 2022). Some studies have suggested that high-spatial-resolution images and maps are required for small croplands within China (Li et al., 2017; Zhai et al., 2021).

Many studies have used time series images at high spatial resolution from single satellite sensors, but their potential for large-scale cropping intensity mapping at high spatial resolution was limited (Li et al., 2017; Yan et al., 2019). Several researches have integrated satellite data from two or more sensors operating at different spatiotemporal resolutions to construct time-series datasets (Li et al., 2017). The Sentinel-2A/B satellites carry wide-swath, multi-spectral imagers (MSI) with 13 spectral bands, providing high spatial (10 m) and temporal (10 days) resolution imagery at no cost to users (He et al., 2021a), which is suitable for integration with Landsat imagery due to the similar spatial resolution (Liu et al., 2020). Composite Sentinel-2 and Landsat dataset allows the acquisition of global and high-spatial-resolution imagery at a temporal resolution of less than 5 days, thus provides more observations to

identify cropland changes and seasonal crop status (Griffiths et al., 2019). A few studies have applied this kind of integrated satellite data to extract high-accuracy cropping intensity information for some parts of China (Hao et al., 2019; Liu et al., 2020; Pan et al., 2021). Therefore, such combination among time series Sentinel-2 and Landsat-7/8 imagery presents substantial potential for large-scale cropping intensity mapping, particularly within complex multiple cropping systems like those in Southern China.

Considering current demand as well as the challenges for generating high-resolution and large-scale cropping intensity maps, this study integrated Landsat-7/8 and Sentinal-2 data and exploited a novel algorithm capable of producing annual cropping intensity map with 10 m spatial resolution. The products are anticipated to offer fundamental data for basic research and agricultural planting strategies.

2. Material and methods

2.1. Study area

The study area covers the entire China $(73^\circ 33'-135^\circ 05')$ E, $3^\circ 51'-53^\circ 33'$ N) (Fig. 1). China spans eight temperature zones from north to south, which differs in thermal conditions and crops growth periods (Qian and Lin, 2004). In accordance with natural conditions and agricultural development direction, China was divided into nine agricultural regions. There are significant regional differences in cropping systems, ranging from one to three crops per year, in addition to practices like intercropping and interplanting.

2.2. Data and pre-processing

2.2.1. NLCD cropland data

We used the cropland layer of 2015 National Land Cover Database

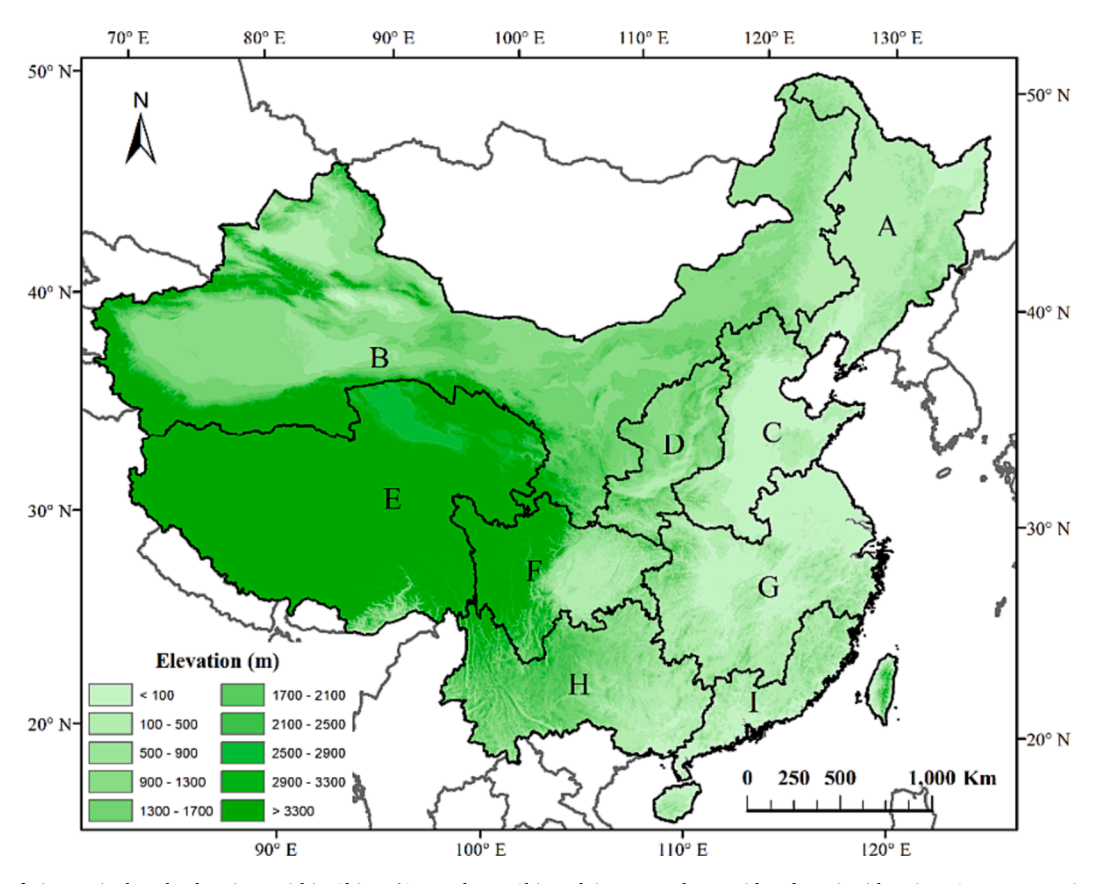


Fig. 1. Locations of nine agricultural subregions within China. (A, Northeast China Plain; B, Northern arid and semi-arid region; C, Huang-Huai-Hai Plain; D, Loess Plateau; E, Qinghai-Tibet Plateau; F, Sichuan Basin and surrounding regions; G, Yangtze Plain; H, Yunnan-Guizhou Plateau; I, Southern China.).

(NLCD). The NLCD-China dataset, developed by Chinese Academy of Sciences via classification of Landsat imagery, had high accuracy, because of a large amount of ground reference data (Liu et al., 2005). As shown in Fig. 2, Large areas of cropland in China are located on several plains, including the Huang-Huai-Hai Plain, Northeast China Plain, Yangtze Plain, and Sichuan Basin, where moderate- and large-size crop fields dominate. In addition, the mountainous and hilly areas of South China is featured with small-size crop fields.

2.2.2. Satellite imagery

To capture the complete planting information of cropland, we utilized integrated Landsat and Sentinel time-series data from August 2016 to July 2018. This time-period was selected because some winter crops, including winter wheat, rapeseed, and oats, were sown during the close of the preceding year and harvested at the beginning of the following year. We obtained top-of-atmosphere (TOA) reflectance dataset of Sentinel-2 MSI, Landsat-7 Enhanced Thematic Mapper Plus (ETM +) and Landsat-8 Operational Land Imager (OLI) from Google Earth Engine (GEE).

We used the F-mask algorithm to identify and remove poor-quality observations containing clouds, cloud shadows, and snow, which significantly affect spectral bands of optical sensors (Zhu et al., 2015). We also used metadata to detect Landsat-7 ETM + scan line corrector (SLC)-off gaps that resulted in missing observations data (Long et al., 2013).

We compared the good-quality observations amount per pixel among each data sources (Fig. 3). Landsat-7 provided smallest amount of good-quality observations per pixel of less than 20 among four data sources.

The combination among Landsat-7/8 and Sentinel-2 time-series dataset provides 10-210 good-quality observations per pixel, with 50.76 % of pixels having over 100 good-quality observations.

Because MSI, ETM + and OLI sensors differ in their imaging methods, spectral range, and spatial resolution, normalization of images from these different sensors is essential before compositing (Nguyen et al., 2020). We selected OLI data as the wavelength standard and utilized ordinary least-squares regression coefficient to transform blue, red, near infrared (NIR), and shortwave infrared (SWIR) bands of MSI and ETM + dataset (Roy et al., 2016). To reconcile the differences in spatial resolutions between Sentinel-2 and Landsat, we applied a bicubic method to resample each band of the ETM+, and OLI data to 10 m \times 10 m.

2.2.3. National statistics data

We used the national cropland and sowing area statistics for 2017 at prefecture-level city scale to evaluate our cropland intensity maps. These statistical data were summarized by professional field surveys and can be accessed from National Bureau of Statistics of China.

2.2.4. Existing cropping intensity maps of China

We collected available cropping intensity maps which covered China for comparison in the Discussion section. (1) The FS02 dataset is generated based on agricultural census statistics and a land cover map, including 0.5° resolution maps of rice paddy and its rotations, and a database contains difference cropland rotation area (Frolking et al., 2002). (2) The KW20 dataset consists of planting sequence, growing period and distribution area of various cropping systems on a global scale, derived using monthly growing data (Waha et al., 2020). (3) The

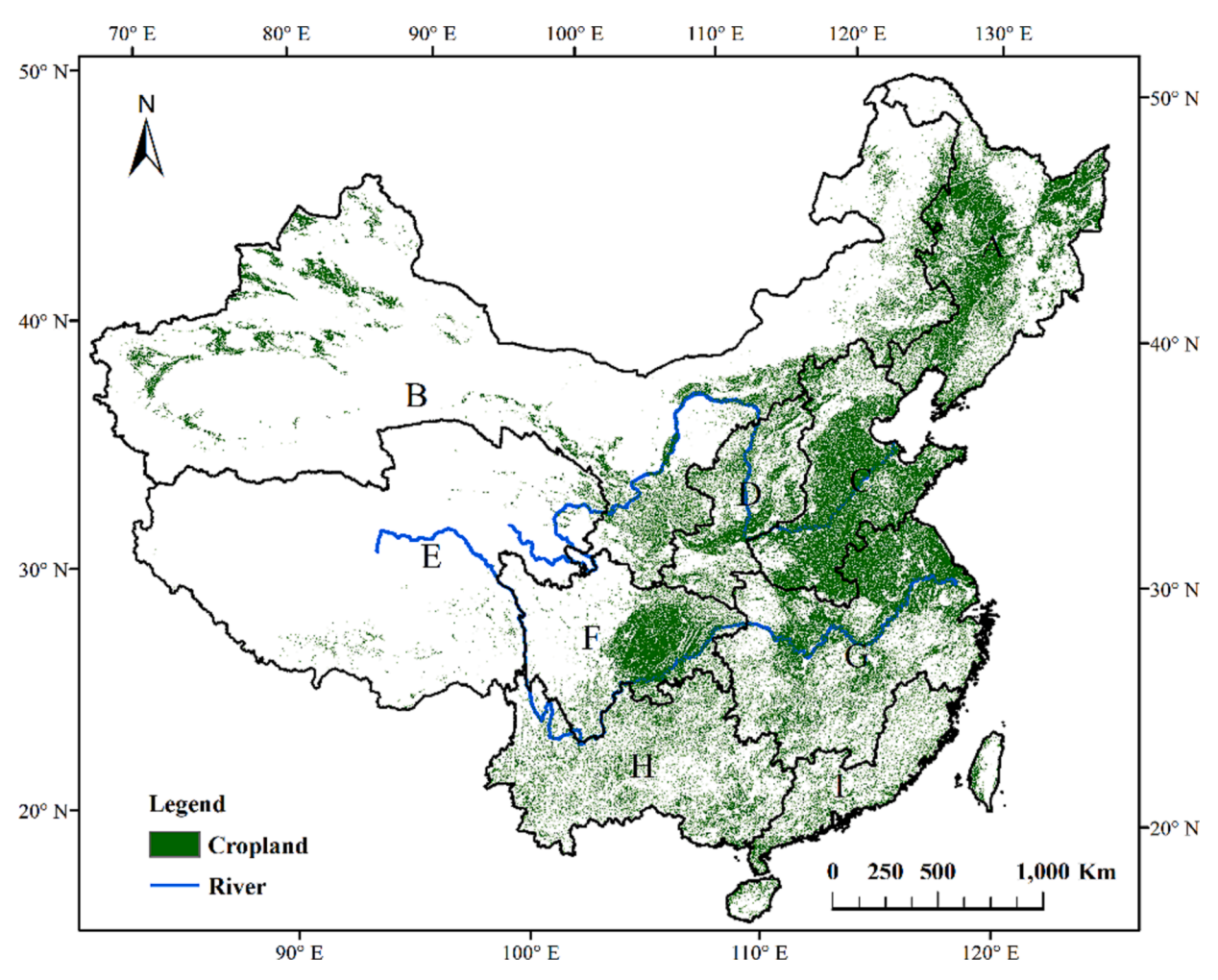


Fig. 2. Distribution of croplands based on 2015 NLCD-China.

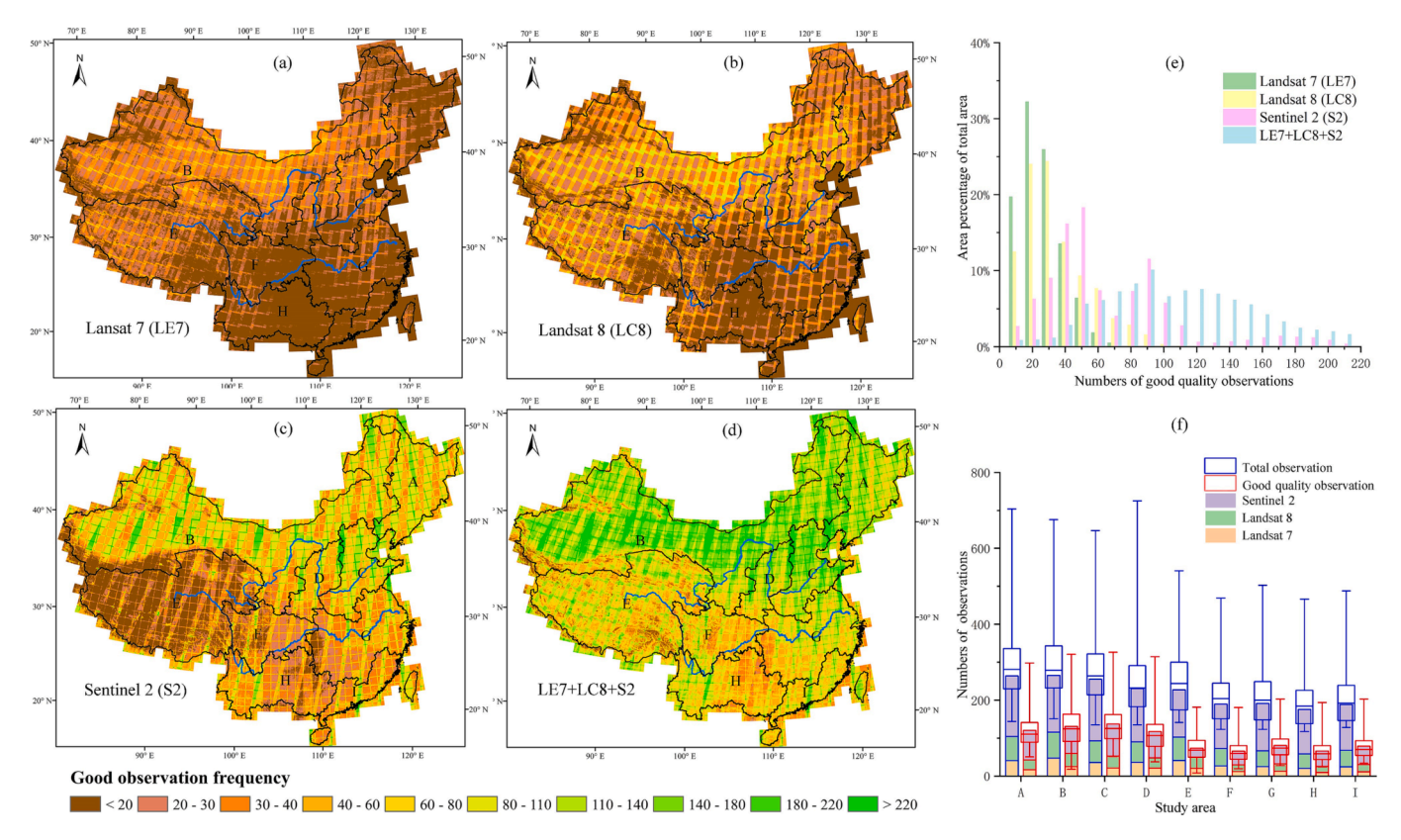


Fig. 3. (a-d) Distributions of good-quality observations per pixel in data obtained from various sensors during the study period. (e) Histograms of area percentage and amount of good-quality observations from various sensors. (f) Total observations and good-quality observations within each agricultural region. Box denotes the maximum, third quartile, median, first quartile, and minimum of total pixels.

YH14 dataset contains China's multiple cropping intensity map for 2002 with 500 m spatial resolution, produced by peak-finding algorithm based on field observations and MODIS data (Yan et al., 2014). (4) The

ZL13 dataset describes multiple cropping index and efficiency of China in 2005 at the 250 m resolution, using decision tree model based on connection between crop phenology and MODIS EVI value (Zuo et al.,

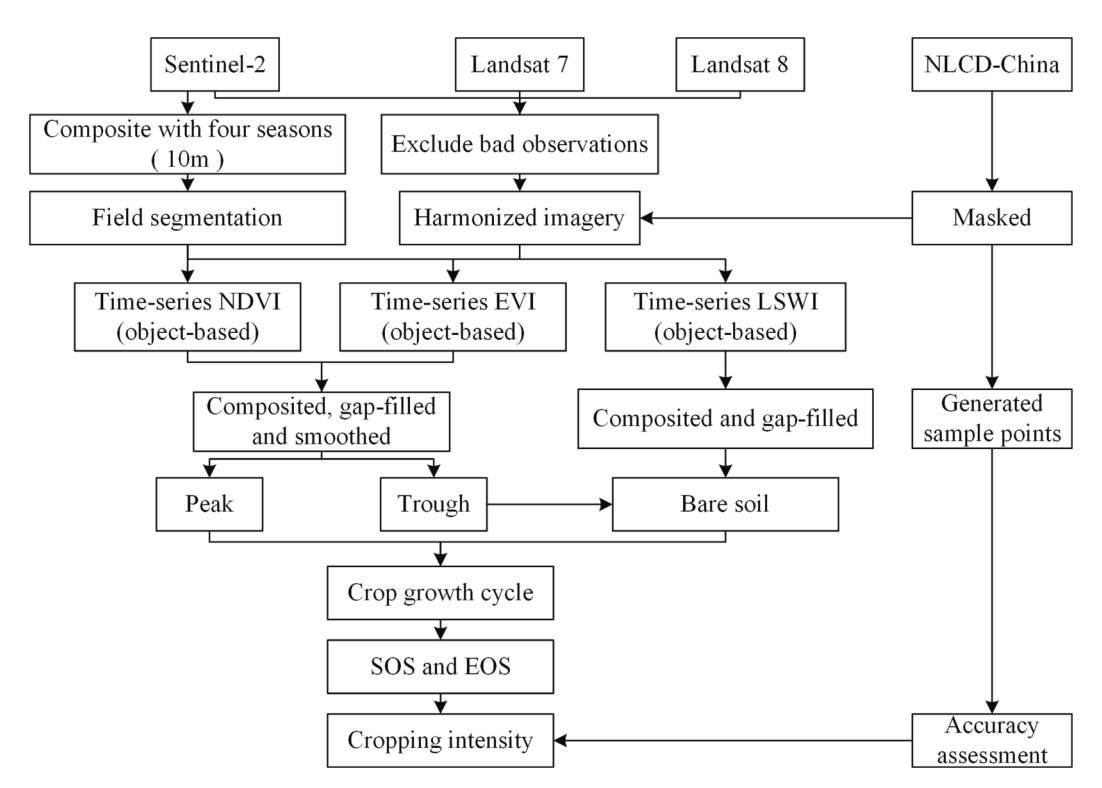


Fig. 4. Data and workflow for phenology- and object-based cropping intensity mapping.

2013). (5) The QB17 dataset includes China's cropping intensity data during 1982–2013 applying wavelet features-based method (Qiu et al., 2017). (6) The GCI30 dataset is a global cropping intensity dataset of 30 m resolution using phenophase-based mapping framework. We calculated the corresponding area proportions and MCI for GCI30 within China based on the dataset provided (Zhang et al., 2021a; Zhang et al., 2021b).

2.3. Method

The data and workflow to produce annual cropping intensity map are shown in Fig. 4. First, cropland data were separated out of the National Land Cover Database for 2015 to make a cropland mask. Second, we calculated three vegetation indexes using preprocessed, integrated Landsat-7/8 and Sentinel-2 dataset with 10 m resolution for each cropland region. We then used an object-based simple non-iterative clustering (SNIC) algorithm to segment crop fields. Third, an algorithm based on peak-finding and thresholds was applied to identify the MCI of each cropland object in China. The accuracy of generated product was evaluated using data collected from a large number of sample points via the cropland mask. Phenological analysis was performed based on visual interpretation. We also compared our results to national statistics in terms of the cropping intensity and spatial distribution in China.

2.3.1. Vegetation index calculation

Identifying alterations in the composition of soils, surface water, and crops over a cropland field is challenging, requiring spectral bands or vegetation indexes that response obviously to these factors (Zhang, 2015). The Normalized Difference Vegetation Index (NDVI) is the most extensively utilized index in cropping studies because it carries information about the canopy growth of crops (Gao et al., 2017; Chen et al., 2018). The Enhanced Vegetation Index (EVI) corrects the effects of aerosol scattering and the soil background. The Land Surface Water Index (LSWI) contains SWIR reflectance, which exhibits sensitivity to soil and crop moisture. We constructed time-series data for these three vegetation indices based on local phenological information and the image acquisition time, using blue, red, NIR, and SWIR spectral bands from the integrated Lansat-7/8 and Sentinel-2 data, as shown in Eqs. (1)–(3):

$$NDVI = \frac{NIR - RED}{NIR + RED} \tag{1}$$

$$EVI = 2.5 \times \frac{NIR - RED}{NIR + 6RED - 7.5BLUE + 1}$$
 (2)

$$LSWI = \frac{NIR - SWIR}{NIR + SWIR}$$
 (3)

where RED, BLUE, NIR, SWIR represent the top of atmosphere reflectance values in TOA imagery of red, blue, near-infrared, short-wave-infrared bands, respectively.

2.3.2. SNIC object-based segmentation

To reduce noise among mixed-pixel time-series data, we performed object-based segmentation to analyze cropping intensity on a large scale. For each of the four seasons (winter, spring, summer, fall), we composited five bands from the Sentinel-2 data: blue, green, red, NIR, and the NDVI. The median values were used to create a layer stack for each season. Then, we used simple non-iterative clustering (SNIC) segmentation algorithm (Achanta and Süsstrunk, 2017), to segment all cropland areas extracted from NLCD-2015. Because SNIC runs within a single iteration and enforces connectivity from the start of the run, it has low memory requirements, high computation efficiency and segmentation quality (Achanta et al., 2012; Achanta and Süsstrunk, 2017). The SNIC algorithm can be implemented on GEE and typically has six parameters. Based on characters of the size and shape in cropland field

parcels for China, the following parameter settings were optimal for cropland region classification (Fig. 5): super-pixel seed location spacing = 6, compactness factor = 5, and connectivity = 8. The same segmentation parameters were used throughout the study area.

2.3.3. Time-series data construction

Average vegetation indices for each image were calculated for the cropland object. To minimize subtle differences in object-based vegetation indices among images, maximum NDVI and EVI composites, and mean LSWI composite were computed for each 10-day period.

We filled the data gaps for each cropland object in images caused by cloud cover using time-series linear interpolation of valid data. Noise generated by cloud, snow, and other factors lead to dramatic fluctuations in NDVI and EVI time-series data, which complicates the analysis and extraction of crop seasonal characteristics (Fischer et al., 2002). Therefore, we denoised and reconstructed the NDVI and EVI datasets using the Savitzky-Golay filter (Fig. 6). Thus, gap-filled and smoothed composite vegetation indices dataset was generated for each cropland object.

2.3.4. An object-based cropping intensity algorithm

Pixel-based phenological and threshold algorithms have been used successfully to extract cropping intensity values for several climate regimes and irrigation management types at various spatial scales in China (Liu et al., 2020). The object-based cropping intensity algorithm is built upon this algorithm incorporating cropland objects into the analysis. NDVI and EVI values gradually increase as a crop enters the growth stage; both reach their peaks when the crop canopy is closed. As the crop enters the reproductive growth stage, NDVI and EVI begin to decline until harvest (Fig. 7). Thus, for each index, values before and after a given time point can be compared to identify the peaks and troughs for a given cropland object.

As winter crops enter the hibernation period, NDVI values begin to decline, resulting in double peaks in the NDVI curve. A similar phenomenon occurs when there is weed growth prior to the planting of a single crop. We applied the dynamic threshold method to distinguish these two phenomena using the LSWI time-series curve (Dong et al., 2015). First, the potential LSWI (T_p) threshold was calculated using Eq. (4), based on the maximum and minimum LSWI values (LSWI_{max} and LSWI_{min}, respectively). Second, the final threshold (T_p) was calculated using Eq. (5), based on maximum and minimum T_p of 0.2 and 0, respectively, in consideration of the difference in soil moisture between South and North China. Finally, LSWI was compared to (T_p) to identify periods when the soil was bare (LSWI < T_p).

$$T_P = LSWI_{min} + (LSWI_{max} - LSWI_{min}) \times 0.15$$
(4)

$$T_F = \begin{cases} 0, T_P < 0 \\ T_P, 0 \le T_P \le 0.2 \\ 0.2, T_P > 0.2 \end{cases}$$
 (5)

However, in some regions of China, when the early rice is harvested, the second rice crop is planted within 2 weeks. The bare soil could not be detected due to the abrupt increase in LSWI. Therefore, we applied an optimized supplementary algorithm to determine whether the period between crop harvesting and planting was short. When time-series NDVI data contained two neighboring peaks, if the LSWI was larger than the NDVI or EVI within a trough between two peaks, then both peaks were considered to represent crop growth (Dong et al., 2016).

Because some non-crop plants may grow, we set a threshold for NDVI $_{max}$ to 0.5 during the plant growth cycle. For each object, if NDVI $_{max} \geq$ 0.5, the object was defined as crop cover; and if NDVI $_{max} <$ 0.5, the object was defined as having no crop cover.

Based on these definitions of crops growth, we used NDVI ratio to detect the start (SOS) and end of season (EOS) according to remaining peaks with crop cover (Mishra et al., 2021), as follows:

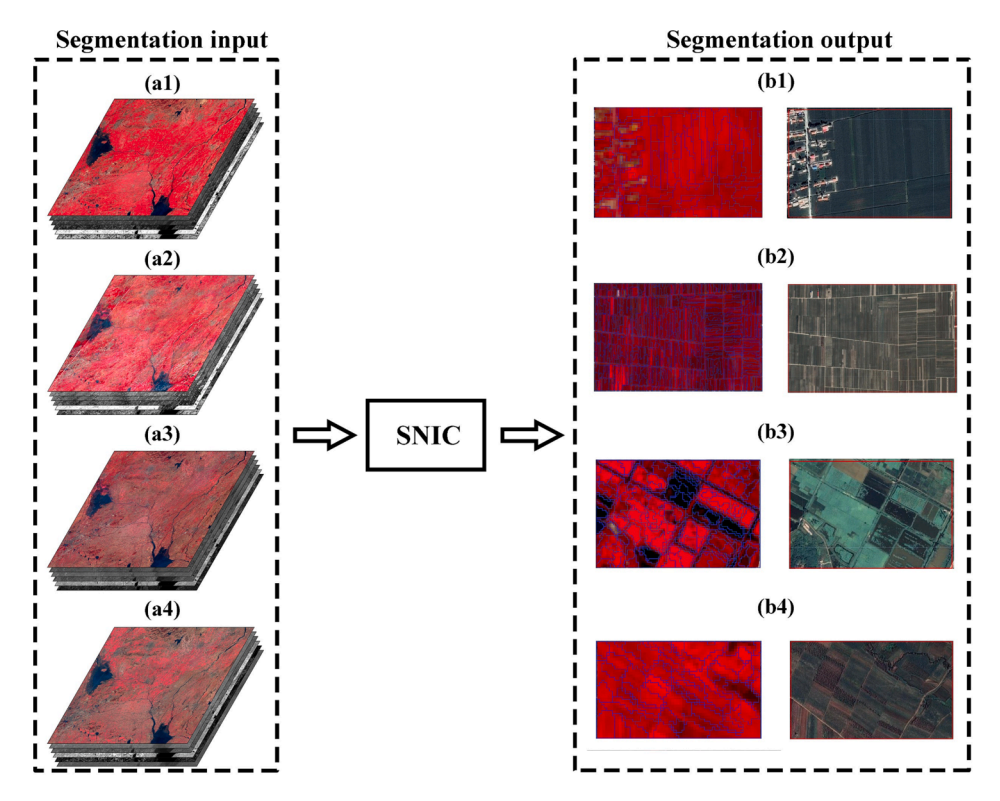


Fig. 5. Simple non-iterative clustering (SNIC) object-based cropland segmentation. (a) Median composite images composed of blue, red, NIR bands and NDVI for each season: (1) spring (March–May 2017), (2) summer (June–August 2017), (3) autumn (September–November 2017), and (4) winter (December 2017 to February 2018). (b) Segmentation results and Google Earth images: located at (1) 125.1839° E, 43.6368° N, (2) 115.3938° E, 38.6803° N, (3) 115.1250° E, 30.1088° N, and (4) 110.0370° E, 21.2697° N. (For interpretation of the references to color in this figure legend, the reader is referred to the web version of this article.)

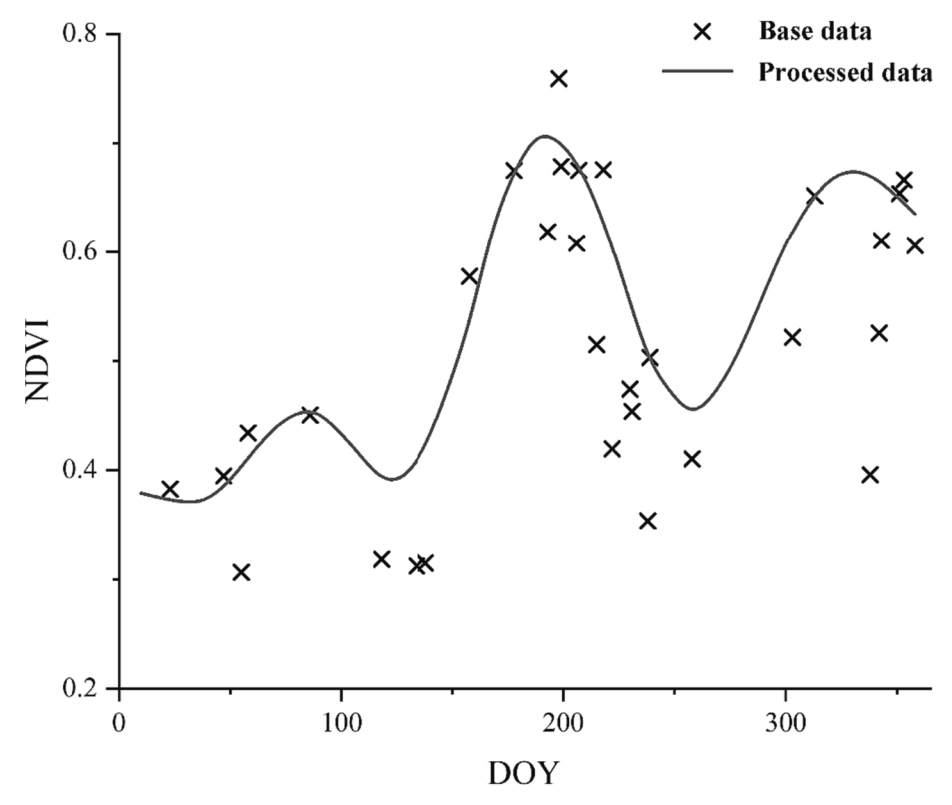


Fig. 6. NDVI time-series data were smoothed using Savitzky-Golay filter.

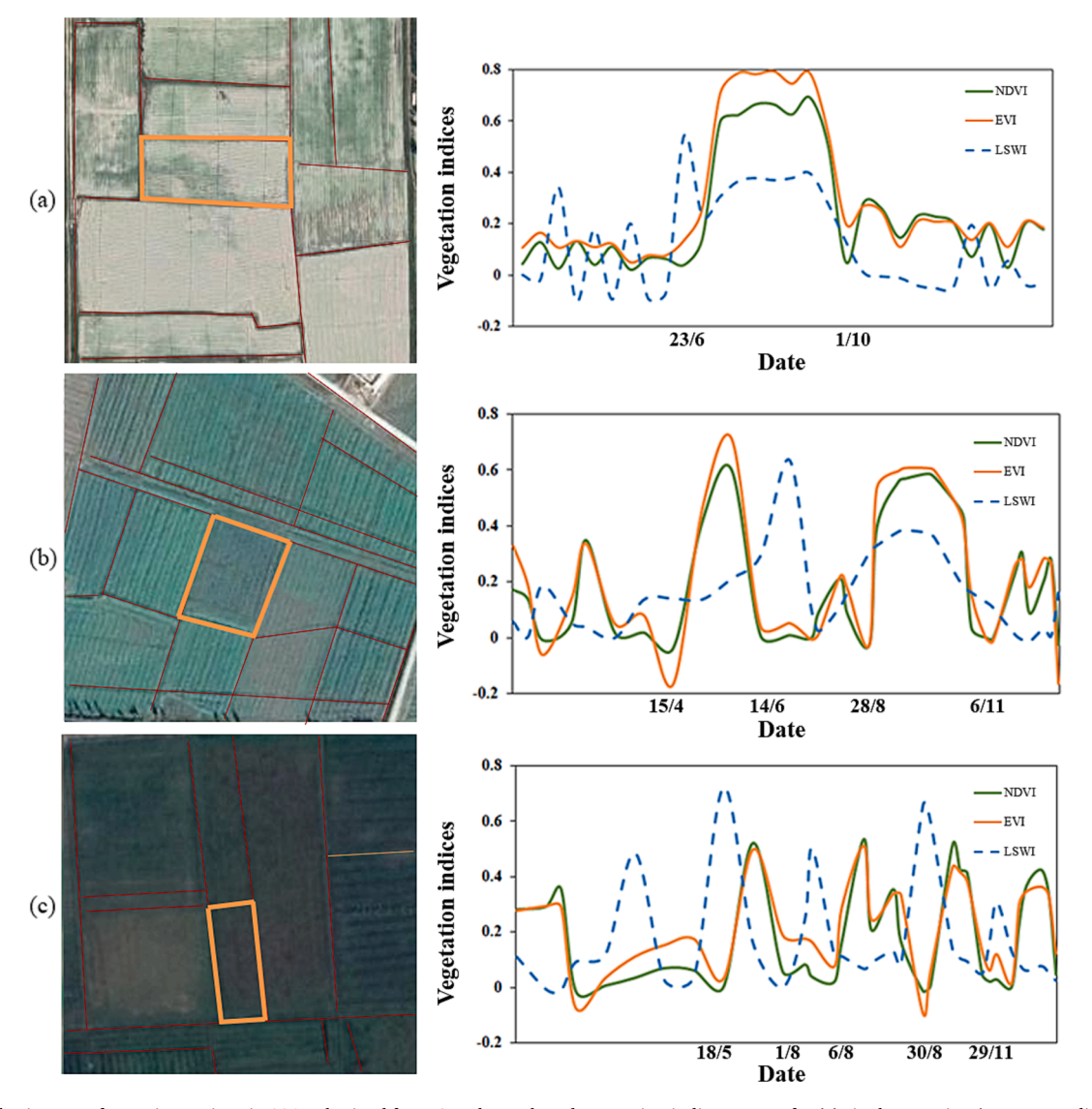


Fig. 7. True color images of cropping regions in 2017 obtained from Google Earth and vegetation indices curves for (a) single-cropping (center coordinates: 86.0829° E, 41.4483° N), (b) double-cropping (center coordinates: 112.8943° E, 23.6309° N), and (c) triple-cropping sample cropland objects (center coordinates: 110.9192° E, 21.5349° N). The red lines indicate the cropland boundaries for object-based segmentation. The orange rectangles indicate the sample cropland objects. (For interpretation of the references to color in this figure legend, the reader is referred to the web version of this article.)

$$NDVI_{ratio} = \frac{NDVI - NDVI_{min}}{NDVI_{max} - NDVI_{min}}$$
(6)

where NDVI_{min} is computed as the minimum NDVI value over a 2-year period. NDVI_{max} is computed as the maximum NDVI value within crops growth duration.

We set SOS as the day when NDVI_{ratio} rised to 0.1, and set EOS as the day when NDVI_{ratio} drop to 0.19, respectively. We determined the MCI by identifying the period when SOS and EOS occurred. When either SOS or EOS of a crop growth cycle occurred during 2017, the MCI was 0.5; when both occurred during 2017, the MCI was 1 (Liu et al., 2020). Finally, we summed and round down the MCI values of all crop growth cycles for each object in 2017, because decimals represent incomplete growth cycles. The cropping intensity map for 2017 was thus created.

2.3.5. Accuracy assessment

We estimated precision following to stratified sampling principle (Olofsson et al., 2014). First, we partitioned cropping intensity map into three strata: single-, double-, and triple-cropping. These three strata accounted for 78 %, 21 %, and 1 % of the cropping intensity map, respectively. The sample size was calculated by stratified random

Table 1Number of sample points in each agricultural region.

Regions	Single cropping	Double cropping	Triple cropping	Total
A	794	10	10	814
В	519	22	10	551
C	402	361	10	773
D	230	24	10	264
E	27	10	10	47
F	349	46	10	405
G	513	271	10	794
H	290	108	10	408
I	120	49	10	179
Total	3244	901	90	4235

sampling (Cochran, 1977). Second, we used the cropland area of the nine agricultural regions to determine sample allocation to three strata (Table 1). In order to ensure that there are a certain number of sample points in three strata of each region, we randomly generated the corresponding number of sample points selected from each of these three strata according to the proportion of regional area (total 4,235 samples).

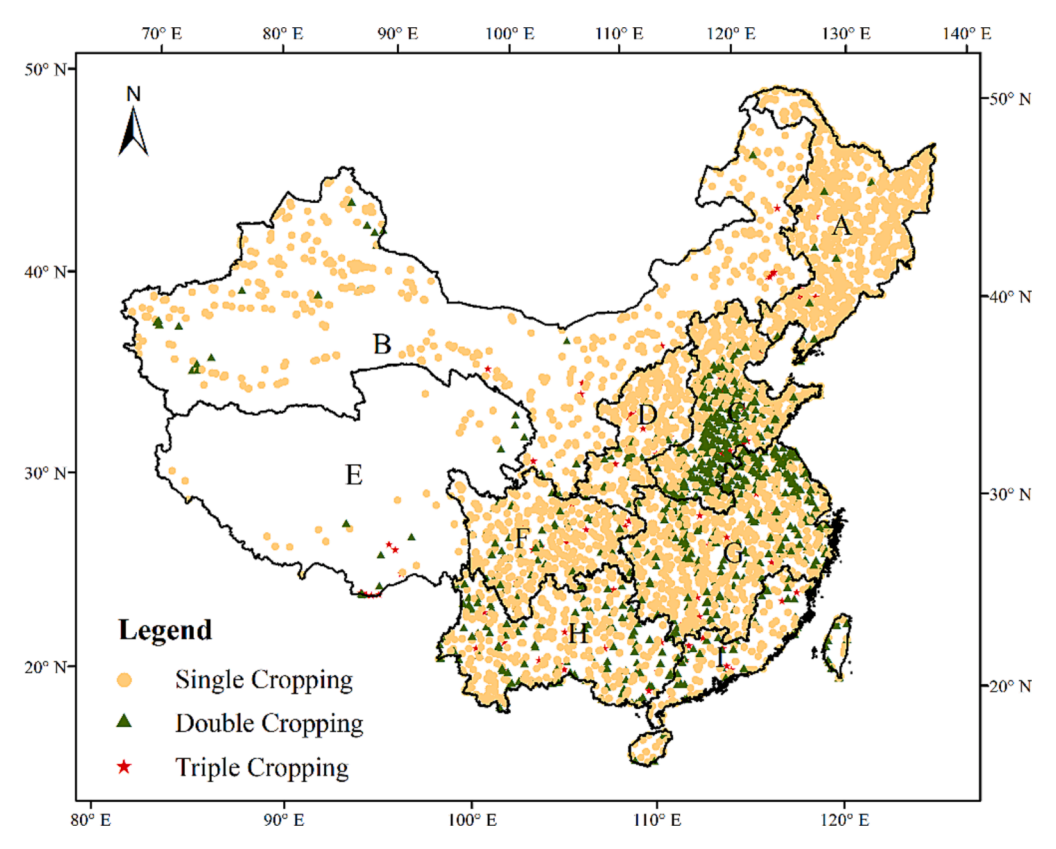


Fig. 8. Ground truth sampling points used for validation.

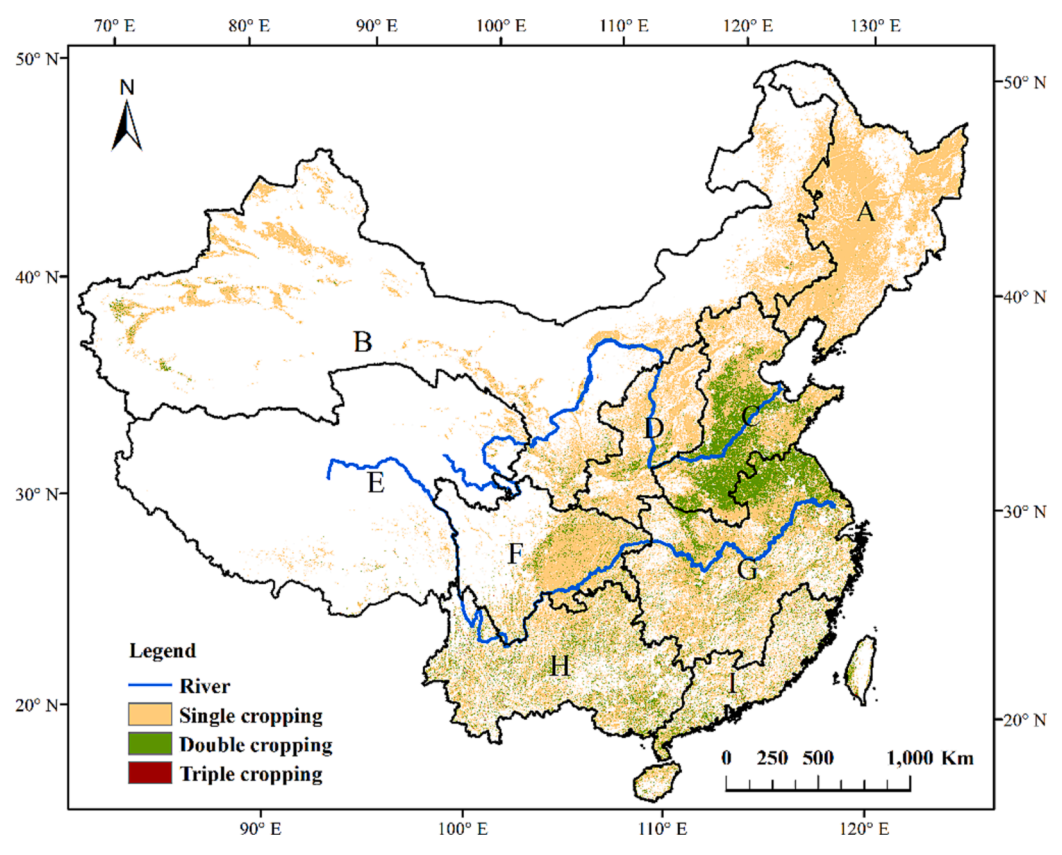


Fig. 9. Annual cropping intensity map in 2017.

Third, we extracted the NDVI, EVI, and LSWI temporal profiles of each sample point from GEE, and distinguished the temporal profiles of the sample points based on visual interpretation and field site data (Fig. 8). Finally, the sample points were overlaid with cropping intensity map, and the cropping intensity information corresponding to the 4,235 sample points was extracted to calculate a confusion matrix for accuracy evaluation and area estimation.

2.3.6. Comparison with national agricultural statistical data

We calculated the estimated area proportions and used these results to estimate the sowing area of each region and prefecture-level city. We also collected regional sowing area data from provincial and prefectural statistical yearbooks published in 2018, which provided statistical data for 2017. We then compared the sowing area data from two different sources. Due to a lack of relevant data in the statistical yearbooks, we excluded some prefectural cities from this analysis. 285 prefectural cities were selected finally for verification.

3. Results

3.1. Area estimates of cropping intensity in 2017

The cropping intensity map shows the distribution of cropping systems within China (Fig. 9). At the national scale, the map estimates a single cropping system area of 1.189 \times 10^6 km² \pm 7.90 \times 10^3 km² (\pm denotes the 95 % confidence interval), accounting for about 79.26 % of the cropland area, followed by a double cropping system area of 0.306 \times 10^6 km² \pm 8.03 \times 10^3 km² (\sim 20.41 %) and triple cropping system area of 5.00 \times 10^3 \pm 1.75 \times 10^3 km² (\sim 0.33 %). By calculation, the national average MCI is 1.21.

The distribution of cropping intensity indicated that cropping systems shifted from single to multiple cropping from north to south. Northern China has generally larger crop fields and more limited thermal conditions; therefore, single cropping is dominant. In comparison, most double-cropping systems clustered within central and southern China, whereas triple-cropping systems scattered sporadically across the southern regions planted with many types of crops with varying growth cycles.

The regional-scale distribution of various cropping system is shown in Table 2. Single cropping systems were mostly found in the Northeast China Plain, accounting for 24.20 % of all single cropping systems area

of the cropping intensity map and 19.18 % of all cropland. Double-cropping systems were majorly found from Huang-Huai-Hai Plain, which accounted for 40.56 % of the double cropping area and 8.28 % of all cropland, respectively. Triple cropping systems were largely distributed across the Yangtze Plain, which accounted for 36.84 % of triple-cropping area and 0.12 % of all cropland, followed by Southern China. The MCI was highest in Huang-Huai-Hai Plain (1.45), followed by Yangtze Plain (1.35) and Southern China (1.34).

Total Single (%), Total Double (%), Total Triple (%) represent single, double-, and triple-cropping area of each region, accounting for the proportion of total single-, double-, and triple-cropping area in China, respectively. Total cropland (%) represents the single-, double-, and triple-cropping area of each region, accounting for the proportion of overall cropland area of China.

3.2. Reliability of annual cropping intensity map

3.2.1. Accuracy based on validation points

The accuracy values for the 2017 annual cropping intensity map of China, obtained using the validation points, are displayed in Table 3. The respective producer and user accuracy (PA, UA) values were 97.36 \pm 0.01 % and 98.58 \pm 0.00 % for single cropping, 94.33 \pm 0.03 % and 89.90 \pm 0.02 % for double cropping, and 78.26 \pm 0.00 % and 84.44 \pm 0.08 % for triple cropping. Therefore, the performance of the phenology-based mapping algorithms declined gradually as the increase of MCI

Table 3Confusion matrix based on validation points in the 2017 cropping intensity map of China derived from the object- and phenology-based algorithm.

Classification	Reference ((validation)	OA	Kappa		
	Single cropping	Double cropping	Triple cropping	UA (%)	(%)	
Single cropping	3198	46	0	$\begin{array}{c} 98.58 \\ \pm \ 0.00 \end{array}$	$96.68 \\ \pm 0.01$	0.90
Double cropping	88	810	3	$\begin{array}{c} 89.90 \\ \pm \ 0.02 \end{array}$		
Triple cropping	0	14	76	$\begin{array}{c} 84.44 \\ \pm \ 0.08 \end{array}$		
PA(%)	97.36 \pm 0.01	$\begin{array}{c} 94.33 \pm \\ 0.03 \end{array}$	$\begin{array}{c} \textbf{78.26} \pm \\ \textbf{0.00} \end{array}$			

Table 2 Statistical summary of cropping system area (10^3 km^2) in each region of China.

	Cropland	Single cropping			Double croppi	ng		Triple crop	pping		MCI
	area	Single area	Total Single	Total cropland	Double area	Total Double	Total cropland	Triple area	Total Triple	Total cropland	
			(%)	(%)		(%)	(%)	_	(%)	(%)	
A	288.97	287.82 ± 0.37	24.20	19.18	1.13 ± 0.37	0.37	0.08	0.02 ± 0.00	0.42	0.00	1.00
В	195.90	187.49 ± 1.56	15.77	12.50	8.20 ± 1.56	2.68	0.55	$\begin{array}{c} \textbf{0.21} \pm\\ \textbf{0.00} \end{array}$	4.20	0.01	1.04
С	276.84	$152.22 \pm \\ 3.78$	12.80	10.15	$\begin{array}{c} 124.20 \pm \\ 3.78 \end{array}$	40.56	8.28	$\begin{array}{c} \textbf{0.42} \pm \\ \textbf{0.09} \end{array}$	8.47	0.03	1.45
D	91.75	$\textbf{84.20} \pm \textbf{1.75}$	7.08	5.61	$\textbf{7.58} \pm \textbf{1.75}$	2.48	0.51	$\begin{array}{c} 0.06 \pm \\ 0.03 \end{array}$	1.26	0.00	1.08
E	10.29	9.72 ± 0.12	0.82	0.65	0.57 ± 0.12	0.19	0.04	$\begin{array}{c} 0.02 \pm \\ 0.00 \end{array}$	0.40	0.00	1.06
F	143.36	$130.67 \pm \\ 2.47$	10.99	8.71	$\begin{array}{c} \textbf{12.48} \pm \\ \textbf{2.47} \end{array}$	4.07	0.83	$\begin{array}{c} \textbf{0.22} \pm \\ \textbf{0.09} \end{array}$	4.34	0.01	1.09
G	285.29	$188.37 \pm \\ 4.19$	15.84	12.56	$\begin{array}{c} 95.08 \pm \\ 4.30 \end{array}$	31.05	6.34	$\begin{array}{c} \textbf{1.84} \pm \\ \textbf{1.03} \end{array}$	36.84	0.12	1.35
Н	145.62	$106.21 \pm \\ 3.27$	8.93	7.08	38.34 ± 3.29	12.52	2.56	$\begin{array}{c} 1.07 \pm \\ 0.35 \end{array}$	21.45	0.07	1.28
I	62.20	42.40 ± 2.48	3.57	2.83	$\begin{array}{c} \textbf{18.67} \pm \\ \textbf{2.56} \end{array}$	6.10	1.24	$\begin{array}{c} 1.13 \pm \\ 0.73 \end{array}$	22.61	0.08	1.34
Total	1500.20	$1189.10 \pm \\ 7.90$	100.00	79.26	$\begin{array}{c} 306.24 \pm \\ 8.03 \end{array}$	100.00	20.41	$\begin{array}{c} 5.00 \ \pm \\ 1.75 \end{array}$	100.00	0.33	1.21

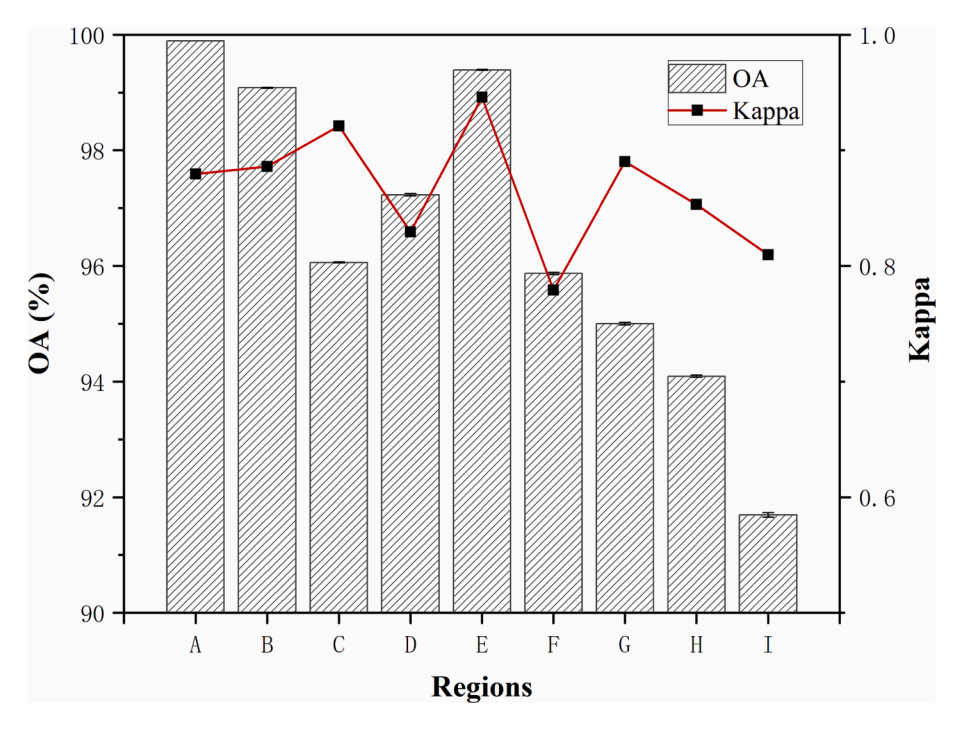


Fig. 10. Accuracy of cropping intensity in each agricultural region of China.

from single- to multiple-cropping regions. The overall accuracy (OA) was 96.68 \pm 0.01 % and the Kappa coefficient was 0.90.

The accuracy of the resulting map for China in 2017 is shown in Fig. 10. The OA varied from 91.69 % to 99.89 %, with a Kappa coefficient range of 0.78–0.94. These reasonably high accuracy values indicate that the improved mapping framework was dependable for 10–30 m scale imagery. From a regional perspective, the Northeast China Plain

had the highest OA (99.89 \pm 0.00 %), and the Qinghai-Tibet Plateau had the highest Kappa (0.95). In addition, The mapping accuracy within northern China was generally greater than within southern regions, which can be attributed to a variety of factors. For example, there was less cloud and rainy weather in northern China during the study period; therefore, more good-quality observations were available in this region.

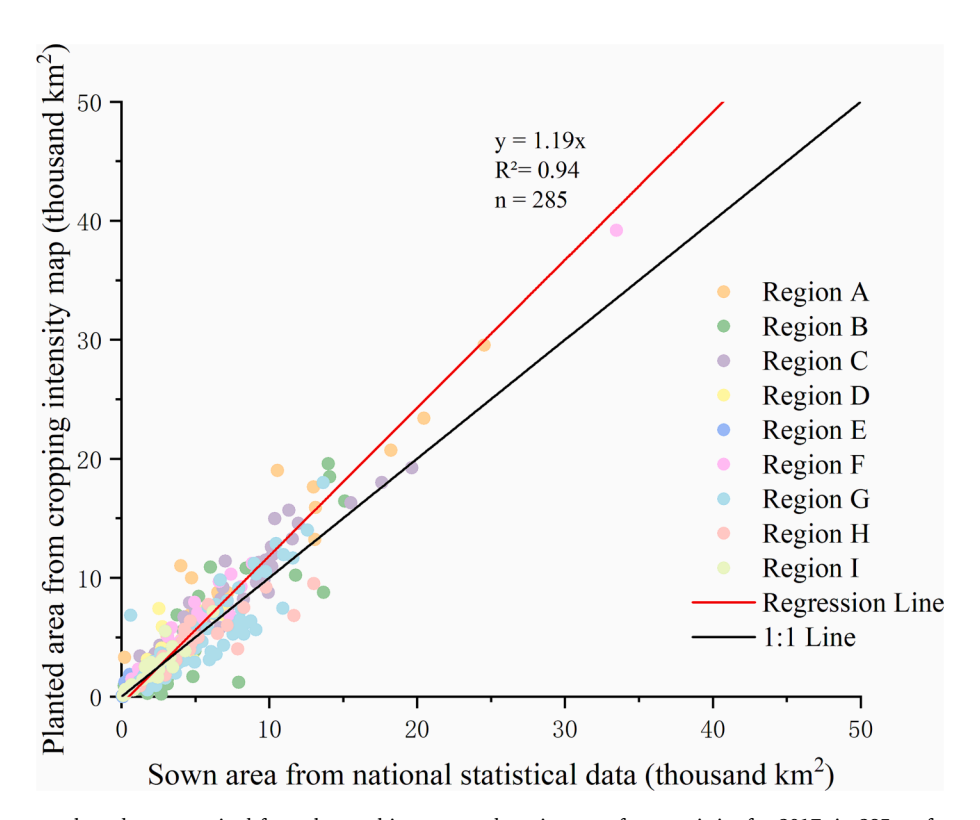


Fig. 11. Comparison between planted area acquired from the resulting map and sowing area from statistics for 2017, in 285 prefectural cities of nine agricultural regions.

3.2.2. Area comparison with national statistics

We compared the 2017 annual cropping intensity map produced in this study with national statistics for 2017 at the prefectural level (285 cities) (Fig. 11). The sowing area calculated from the generated maps and national statistics showed a significant linear relationship (R $^2=0.94$). The mean error (ME) and root mean square error (RMSE) were $3.37\times10^3~{\rm km}^2$ and $6.44\times10^3~{\rm km}^2$, respectively, for the entire study area (Table 4). The sowing area was larger according to the cropping intensity map than the national statistics throughout the study area, mainly because NLCD-China showed a larger cropland area of $1.50\times10^6~{\rm km}^2$ than the national statistical yearbook (1.349 \times 106 km²). The regional evaluation results indicated that the Sichuan Basin and surrounding regions had the strongest correlation while the Qinghai-Tibet Plateau had the weakest correlation.

4. Discussion

4.1. Result comparison with other similar products

According to the 2017 annual cropping intensity map (Fig. 9) and other related products, multiple-cropping area showed substantial changes between previous studies and the present one (Table 5). The proportion of single-cropping systems expanded from 64.0 % to 79.26 % between 2013 and 2017, while that of multiple-cropping systems decreased from 36.0 % to 20.74 % of total cropland. However, in 1995–1996, 1.30×10^6 km² of cropland (~ 30 %) was estimated to be double-cropped, whereas 10 % was triple-cropped. Thus, use patterns of the various cropping systems in China have changed significantly.

Due to the similarity in spatial resolution and study years, the GCI30 dataset was selected for regional-scale comparison with our CI product. The regional comparison results in Table 6 demonstrated that our cropping intensity results resembled GCI30 in most regions of China. The significant differences were primarily observed in Sichuan Basin and surrounding regions as well as Yangtze Plain. In these two regions, the calculated MCI in our study was significantly lower compared to the GCI30 dataset.

To further investigate detailed differences between the two products, we selected some representative areas within nine agricultural regions in China for comparative analysis (Fig. 12). In the regions characterized by large field parcels and predominantly single-cropping, such as the Northeast China Plain and the Northern arid and semi-arid region, GCI30 and our results showed similar cropping intensity distribution. In certain regions such as the Yunnan-Guizhou Plateau, there were significant differences in cropland boundaries due to different cropland masks used. In the regions such as Southern China and the Huang-Huai-Hai Plain, GCI30 exhibited some fragmented segmentation results and scattered pixel misclassifications, possibly influenced by mixed-pixel at 30 m resolution. However, our object-based approach effectively alleviated such issues and performed relatively well even in areas with complex climate and small field parcels.

4.2. Advantages and limitations of our approaches

Previously, we reported inaccuracies in "salt and pepper" pixels, which resulted from the noise in the mixed-pixel data from data source (Liu et al., 2020). Moreover, the pixel-based mismatches over the time-series Sentinel-2 data should also be noted (Yan et al., 2018). Therefore, we used the object-based SNIC segmentation algorithm to divide

cropland area into field objects. This approach greatly alleviated the problem of Sentinel-2 Level-2A pixel dimension mismatches across time, and significantly improved the accuracy of the cropping intensity map (Table 7). The OA and the Kappa coefficient increased to 97 % and 0.90, respectively.

The time-series remote sensing data used in recent studies for crop intensity mapping have obvious limitations (Li and Roy, 2017). For instance, MODIS images with low spatial resolution are usually adopted for cropping intensity mapping in China (Wu et al., 2018; Mishra et al., 2021). However, low-spatial-resolution remote sensing data contain many mixed pixels, which influences the accuracy of cropping intensity mapping (Bégué et al., 2018; Tran et al., 2022). Our study integrated Landsat-7/8, and Sentinel-2 times-series dataset to generate 10-m cropping intensity maps with high temporal high temporal frequency. Compared to works that used only Landsat or Sentinel-2 data, the integrated data substantially expanded the quantity of high-quality observations, which is especially significant for field-scale practical applications (Yu et al., 2015).

We selected several areas for comparison of the CI maps from only Sentinel-2 and from integrated multi-source data (Fig. 13). In areas with low cloud cover, such as the Yangtze River Plain, the results obtained from two kinds of data source showed small differences. But in the regions with high cloud cover, such as Sichuan Province, the exclusive use of Sentinel-2 data could not overcome the problem of data gaps, leading to significant underestimation of area of double or triple cropping. In summary, the integration of multi-source data enhanced the probability of capturing critical phenological periods of crops and subsequently improving accuracy. However, our integration algorithm still had limitations. Despite images from different sensors were normalized, spectral inconsistency persisted among them. Therefore, the inclusion of multisource data in the areas with fewer clouds could also introduce subtle noise.

Our study area has a complex topography and a wide variety of climate characteristics. Landsat 7/8 imagery of 30 m resolution may contain many mixed pixels representing various land cover types, despite resampling to a 10 m resolution, which is a major potential source of error in cropping intensity mapping.

4.3. Implications and future work

Many factors drive shifts of distribution and area of multiple cropping patterns within China, including natural, socioeconomic, agricultural, labor, and governmental factors (Liu, 2018; Liu et al., 2021). For example, shifts in multiple-cropping patterns have been shown to be influenced by socioeconomic factors and be spatiotemporally coupled with urbanization (Qiu et al., 2020). Detailed information on cropping intensity and further research on driving factors are essential for understanding these changes in agricultural systems (Chen et al., 2020). Besides, deep learning techniques can be included to improve the fusing of multi-source remote sensing dataset and cropping intensity mapping at a larger scale. Our future studies will be oriented towards these directions.

5. Conclusion

We put forward a novel object- and phenology-based framework to map annual cropping intensity with 10 m resolution within China implemented on GEE. The generated cropping intensity map obtained

Table 4Correlation between planted area (\times 10³ km²) acquired from the resulting map and sowing area (\times 10³ km²) from statistics for 2017 in nine agricultural regions.

	Α	В	С	D	E	F	G	Н	I	Total
ME	3.37	1.66	1.48	1.19	0.44	1.58	1.20	1.14	0.47	1.43
RMSE	6.44	2.36	1.87	1.66	0.65	2.02	1.65	1.65	0.69	2.59
R ²	0.97	0.78	0.91	0.62	0.25	0.98	0.79	0.72	0.83	0.94

Table 5Proportions of various cropping intensity categories in China from different study.

		FS02 (Frolking et al., 2002)	KW20 (Waha et al., 2020)	YH14 (Yan et al., 2014)	ZL13 (Zuo et al., 2013)	QB17 (Qiu et al., 2017)	GCI30 (Zhang et al., 2021b)	Our study
Study p	eriod	1990–1996	1998-2002	2002	2005	2013	2016-2018	2017
Spatial	resolution	0.5°	30 arcmin	500 m	250 m	unknown	30 m	10 m
Area	Single	61.7	64.0	66.0	54.0	64.0	74.98	79.26
(%)	Double	27.4	35.7	32.2	39.0	32.8	24.58	20.41
	Triple	10.9	0.3	1.8	7.0	3.2	0.44	0.33
MCI of	China	1.49	1.36	1.36	1.53	1.39	1.25	1.21

Table 6
Regional MCI comparison in China of our results and GCI30 (Zhang et al., 2021b).

						Regions	Regions				
·			A	В	C	D	E	F	G	Н	I
GCI30	Cropping area ratio of cropland(%)	Single	99.91	96.79	52.36	87.70	95.30	77.25	54.42	64.45	45.58
		Double	0.09	3.20	46.16	12.16	4.67	22.60	45.22	35.20	52.56
		Triple	0.00	0.00	1.48	0.14	0.03	0.15	0.36	0.35	1.87
	MCI of Region		1.00	1.03	1.49	1.12	1.05	1.23	1.46	1.36	1.56
Our study	Cropping area ratio of cropland(%)	Single	99.60	95.71	54.98	91.77	94.46	91.15	66.03	72.94	68.17
		Double	0.39	4.19	44.86	8.26	5.54	8.71	33.33	26.33	30.02
		Triple	0.01	0.11	0.15	0.07	0.19	0.15	0.64	0.73	1.82
	MCI of Region		1.00	1.04	1.45	1.08	1.06	1.09	1.35	1.28	1.34

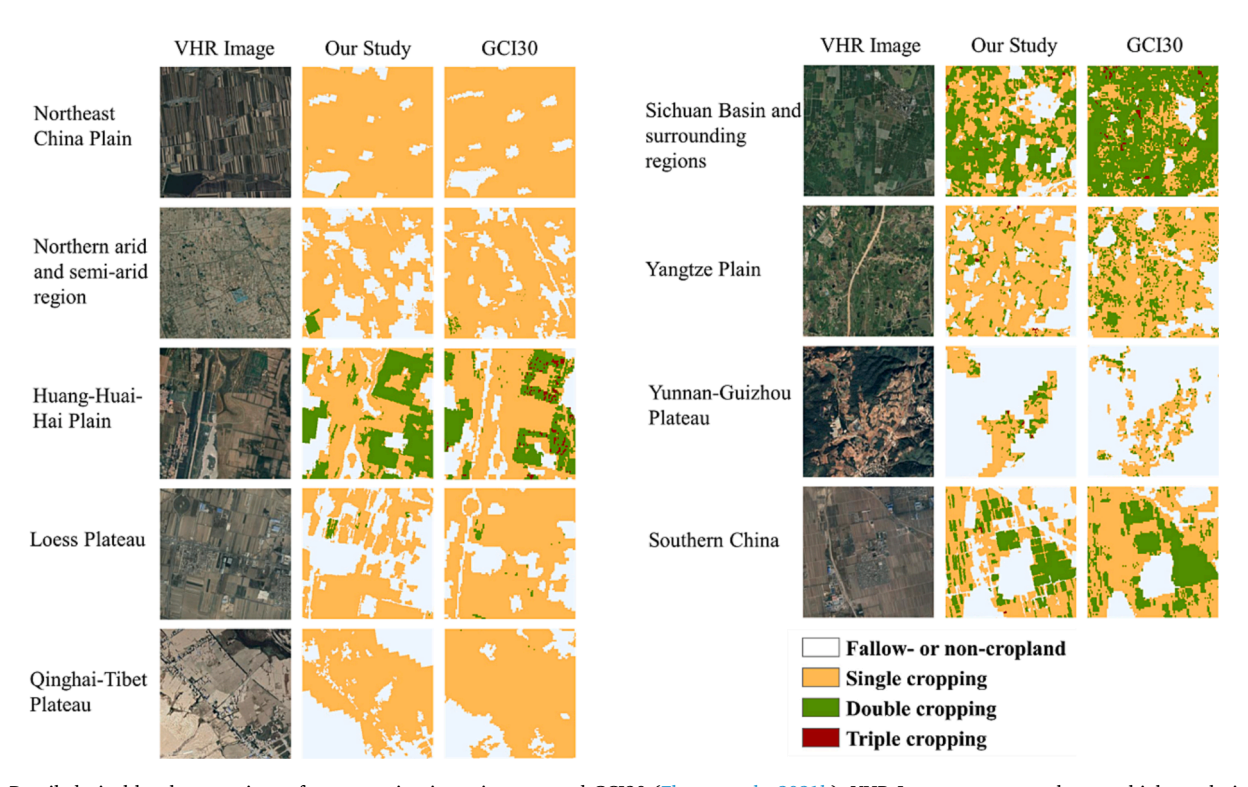


Fig. 12. Detailed pixel-level comparison of our cropping intensity map and GCI30 (Zhang et al., 2021b). VHR Image represents the vary high resolution image obtained from GEE.

Table 7Comparison between accuracy of the cropping intensity map generated using the improved algorithm developed in the present study and that of our previous study (Liu et al., 2020).

Algorithm	Accuracy assessment			
	OA	Карра		
pixel-based	93 %	0.84		
object-based	97 %	0.90		

by identifying crop growth cycles showed high accuracy with an OA of 96.68 \pm 0.01 % and a Kappa coefficient of 0.90. In addition, it significantly alleviated mixed-pixel effects and provided spatial data with more detailed information particularly for smallholder farms in Southern China. The proposed algorithm has broad application prospects based on high availability and repeatability.

CRediT authorship contribution statement

Luo Liu: Conceptualization, Methodology, Software, Data curation.

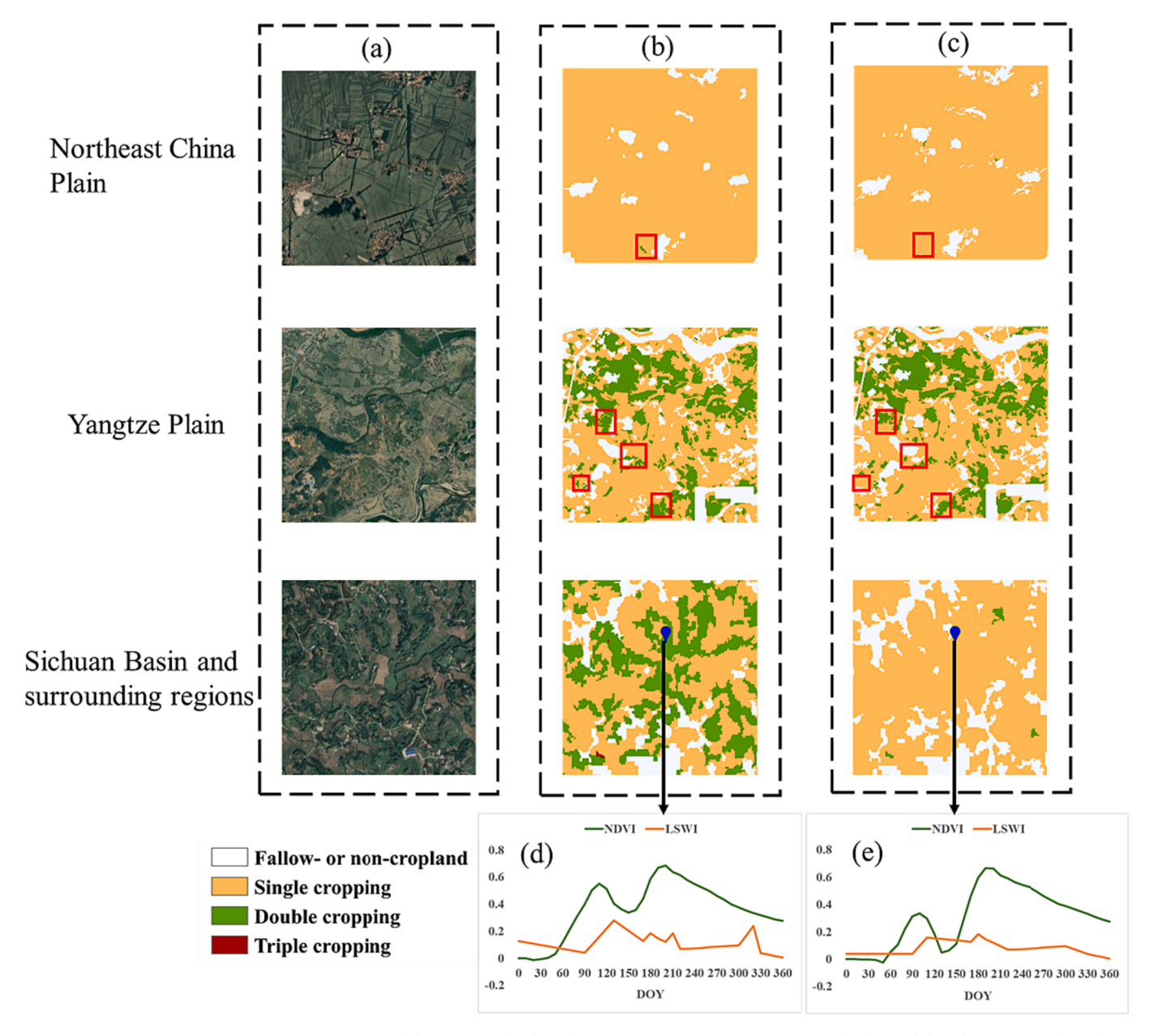


Fig. 13. Comparison of cropping intensity mapping result between two kinds of data source: (a) VHR Images from GEE, (b) the result based on integrated Landsat-7/8 and Sentinel-2, (c) the result based on Sentinel-2, and (d, e) NDVI and LSWI temporal profiles of a sample point located at 106.3131° E, 30.8861° N.

Shangui Kang: Visualization, Data curation, Validation, Writing - review & editing. Xiliu Xiong: Writing - original draft, Software, Validation. Yuanwei Qin: Conceptualization, Resources. Jie Wang: Methodology, Investigation. Zhenjie Liu: Validation, Software. Xiangming Xiao: Resources, Supervision, Funding acquisition, Data curation, Writing - review & editing.

Declaration of Competing Interest

The authors declare that they have no known competing financial interests or personal relationships that could have appeared to influence the work reported in this paper.

Data availability

Data will be made available on request.

Acknowledgments

This study was in part supported by research grants from the National Natural Science Foundation of China (81961128002) and the U.S. National Science Foundation (1911955, 2200310).

References

Achanta, R., Shaji, A., Smith, K., Lucchi, A., Fua, P., Susstrunk, S., 2012. SLIC superpixels compared to state-of-the-art superpixel methods. IEEE Transactions on Pattern Analysis and Machine Intelligence 34, 2274–2282.

Achanta, R., Susstrunk, S., 2017. Superpixels and polygons using simple non-iterative clustering. In: Proceedings of the IEEE Conference on Computer Vision and Pattern Recognition, pp. 4651–4660.

Bégué, A., Arvor, D., Bellon, B., Betbeder, J., De Abelleyra, D., PD Ferraz, R., Lebourgeois, V., Lelong, C., Simões, M., R Verón, S., 2018. Remote sensing and cropping practices: A review. Remote Sens. 10, 99.

Chen, Y., Lu, D., Moran, E., Batistella, M., Dutra, L.V., Sanches, I.D.A., Da Silva, R.F.B., Huang, J., Luiz, A.J.B., De Oliveira, M.A.F.O., 2018. Mapping croplands, cropping patterns, and crop types using MODIS time-series data. International Journal of Applied Earth Observation and Geoinformation 69, 133–147.

- Chen, C., van Groenigen, K.J., Yang, H., Hungate, B.A., Yang, B., Tian, Y., Chen, J., Dong, W., Huang, S., Deng, A., 2020. Global warming and shifts in cropping systems together reduce China's rice production. Global Food Secur. 24, 100359.
- Cochran, W.G., 1977. Sampling techniques, 3rd Edition. Wiley.
- Ding, M., Chen, Q., Xin, L., Li, L., Li, X., 2015. Spatial and temporal variations of multiple cropping index in China based on SPOT-NDVI during 1999–2013. Acta Geogr. Sin 70, 1080–1090.
- Doelman, J.C., Stehfest, E., Tabeau, A., van Meijl, H., 2019. Making the Paris agreement climate targets consistent with food security objectives. Global Food Secur. 23, 93–103.
- Dong, J., Xiao, X., Kou, W., Qin, Y., Zhang, G., Li, L., Jin, C., Zhou, Y., Wang, J., Biradar, C., 2015. Tracking the dynamics of paddy rice planting area in 1986–2010 through time series Landsat images and phenology-based algorithms. Remote Sensing of Environment 160, 99–113.
- Dong, J., Xiao, X., Menarguez, M.A., Zhang, G., Qin, Y., Thau, D., Biradar, C., Moore III, B., 2016. Mapping paddy rice planting area in northeastern Asia with Landsat 8 images, phenology-based algorithm and Google Earth Engine. Remote Sensing of Environment 185, 142–154.
- FAOSTAT, 2018. FAOSTAT database, Food and Agriculture Organization of the United Nations.
- Fischer, G., Velthuizen, H.V., Shah, M., Nachtergaele, F., 2002. Global Agro-ecological Assessment for Agriculture in the 21st Century: Methodology and Results. IIASA RR-02-02.
- Frolking, S., Qiu, J., Boles, S., Xiao, X., Liu, J., Zhuang, Y., Li, C., Qin, X., 2002. Combining remote sensing and ground census data to develop new maps of the distribution of rice agriculture in China. Global Biogeochemical Cycles 16.
- Gao, F., Anderson, M.C., Zhang, X., Yang, Z., Alfieri, J.G., Kustas, W.P., Mueller, R., Johnson, D.M., Prueger, J.H., 2017. Toward mapping crop progress at field scales through fusion of Landsat and MODIS imagery. Remote Sensing of Environment 188, 0.05
- Griffiths, P., Nendel, C., Hostert, P., 2019. Intra-annual reflectance composites from Sentinel-2 and Landsat for national-scale crop and land cover mapping. Remote Sensing of Environment 220, 135–151.
- Hao, P., Tang, H., Chen, Z., Le, Y., Wu, M., 2019. High resolution crop intensity mapping using harmonized Landsat-8 and Sentinel-2 data. Journal of Integrative Agriculture 18, 2883–2897.
- He, Y., Dong, J., Liao, X., Sun, L., Wang, Z., You, N., Li, Z., Fu, P., 2021a. Examining rice distribution and cropping intensity in a mixed single-and double-cropping region in South China using all available Sentinel 1/2 images. International Journal of Applied Earth Observation and Geoinformation 101. 102351.
- He, Z., Li, S., Deng, Y., Zhai, P., Hu, Y., 2021b. Rice paddy fields identification based on backscatter features of Quad-Pol Radarsat-2 data and simple decision tree method. IEEE International Geoscience and Remote Sensing Symposium 6765–6768.
- He, C., Liu, Z., Xu, M., Ma, Q., Dou, Y., 2017. Urban expansion brought stress to food security in China: Evidence from decreased cropland net primary productivity. The Science of the Total Environment 576, 660–670.
- Kogan, F., 2019. Remote sensing for food security. Springer.
- Li, J., Roy, D.P., 2017. A global analysis of Sentinel-2A, Sentinel-2B and Landsat-8 data revisit intervals and implications for terrestrial monitoring. Remote Sens. 9, 902.
- Li, Q., Wang, C., Zhang, B., Lu, L., 2015. Object-based crop classification with Landsat-MODIS enhanced time-series data. Remote Sens. 7, 16091–16107.
- Li, Y., Wu, W., Liu, Y., 2018. Land consolidation for rural sustainability in China: Practical reflections and policy implications. Land Use Policy 74, 137–141.
- Li, L., Zhao, Y., Fu, Y., Pan, Y., Yu, L., Xin, Q., 2017. High resolution mapping of cropping cycles by fusion of landsat and MODIS data. Remote Sens. 9, 1232.
- Lin, F., Li, X., Jia, N., Feng, F., Huang, H., Huang, J., Fan, S., Ciais, P., Song, X.-P., 2023. The impact of Russia-Ukraine conflict on global food security. Global Food Secur. 36, 100661
- Liu, Y., 2018. Introduction to land use and rural sustainability in China. Land Use Policy 74, 1–4.
- Liu, J., Liu, M., Tian, H., Zhuang, D., Zhang, Z., Zhang, W., Tang, X., Deng, X., 2005. Spatial and temporal patterns of China's cropland during 1990–2000: an analysis based on Landsat TM data. Remote Sensing of Environment 98, 442–456.
- Liu, X., Liu, Y., Liu, Z., Chen, Z., 2021. Impacts of climatic warming on cropping system borders of China and potential adaptation strategies for regional agriculture development. The Science of the Total Environment 755, 142415.
- Liu, L., Xiao, X., Qin, Y., Wang, J., Qiao, Z., 2020. Mapping cropping intensity in China using time series Landsat and Sentinel-2 images and Google Earth Engine. Remote Sensing of Environment 239, 111624.
- Liu, F., Zhang, Z., Zhao, X., Wang, X., Zuo, L., Wen, Q., Yi, L., Xu, J., Hu, S., Liu, B., 2019. Chinese cropland losses due to urban expansion in the past four decades. The Science of the Total Environment 650, 847–857.
- Liu, F., Xiao, X., Qin, Y., Yan, H., Huang, J., Wu, X., Zhang, Y., Zou, Z., Doughty, R.B., 2022. Large spatial variation and stagnation of cropland gross primary production increases the challenges of sustainable grain production and food security in China. The Science of the Total Environment 811, 151408.
- Long, J.A., Lawrence, R.L., Greenwood, M.C., Marshall, L., Miller, P.R., 2013. Object-oriented crop classification using multitemporal ETM+ SLC-off imagery and random forest. Gisci. Remote Sens. 50, 418–436.
- Mishra, B., Busetto, L., Boschetti, M., Laborte, A., Nelson, A., 2021. RICA: A rice crop calendar for Asia based on MODIS multi year data. International Journal of Applied Earth Observation and Geoinformation 103, 102471.
- Nguyen, M.D., Baez-Villanueva, O.M., Bui, D.D., Nguyen, P.T., Ribbe, L., 2020. Harmonization of Landsat and Sentinel 2 for Crop Monitoring in Drought Prone Areas: Case Studies of Ninh Thuan (Vietnam) and Bekaa (Lebanon). Remote Sens. 12, 281.

- Olofsson, P., Foody, G.M., Herold, M., Stehman, S.V., Woodcock, C.E., Wulder, M.A., 2014. Good practices for estimating area and assessing accuracy of land change. Remote Sensing of Environment 148, 42–57.
- Pan, L., Xia, H., Yang, J., Niu, W., Wang, R., Song, H., Guo, Y., Qin, Y., 2021. Mapping cropping intensity in Huaihe basin using phenology algorithm, all Sentinel-2 and Landsat images in Google Earth Engine. International Journal of Applied Earth Observation and Geoinformation 102, 102376.
- Panigrahy, S., Manjunath, K.R., Ray, S.S., 2005. Deriving cropping system performance indices using remote sensing data and GIS. International Journal of Remote Sensing 26, 2595–2606.
- Peng, D., Huete, A.R., Huang, J., Wang, F., Sun, H., 2011. Detection and estimation of mixed paddy rice cropping patterns with MODIS data. International Journal of Applied Earth Observation and Geoinformation 13, 13–23.
- Qian, W., Lin, X., 2004. Regional trends in recent temperature indices in China. Climate Research 27, 119–134.
- Qiu, B., Lu, D., Tang, Z., Song, D., Zeng, Y., Wang, Z., Chen, C., Chen, N., Huang, H., Xu, W., 2017. Mapping cropping intensity trends in China during 1982–2013. Applied Geography 79, 212–222.
- Qiu, B., Zou, F., Chen, C., Tang, Z., Zhong, J., Yan, X., 2018. Automatic mapping afforestation, cropland reclamation and variations in cropping intensity in central east China during 2001–2016. Ecological Indicators 91, 490–502.
- Qiu, B., Yang, X., Tang, Z., Chen, C., Li, H., Berry, J., 2020. Urban expansion or poor productivity: Explaining regional differences in cropland abandonment in China during the early 21st century. Land Degradation and Development 31, 2540–2551.
- Qiu, B., Lin, D., Chen, C., Yang, P., Tang, Z., Jin, Z., Ye, Z., Zhu, X., Duan, M., Huang, H., Zhao, Z., Xu, W., Chen, Z., 2022. From cropland to cropped field: A robust algorithm for national-scale mapping by fusing time series of Sentinel-1 and Sentinel-2. International Journal of Applied Earth Observation and Geoinformation 113, 103006.
- Roy, D.P., Kovalskyy, V., Zhang, H., Vermote, E.F., Yan, L., Kumar, S., Egorov, A., 2016. Characterization of Landsat-7 to Landsat-8 reflective wavelength and normalized difference vegetation index continuity. Remote Sensing of Environment 185, 57–70.
- Rufin, P., Frantz, D., Ernst, S., Rabe, A., Griffiths, P., Özdoğan, M., Hostert, P., 2019. Mapping cropping practices on a national scale using intra-annual landsat time series binning. Remote Sens. 11, 232.
- Shao, Y., Lunetta, R.S., Wheeler, B., Iiames, J.S., Campbell, J.B., 2016. An evaluation of time-series smoothing algorithms for land-cover classifications using MODIS-NDVI multi-temporal data. Remote Sensing of Environment 174, 258–265.
- Sun, C., Bian, Y., Zhou, T., Pan, J., 2019. Using of multi-source and multi-temporal remote sensing data improves crop-type mapping in the subtropical agriculture region. Sensors 19, 2401.
- Tran, K.H., Zhang, H.K., McMaine, J.T., Zhang, X., Luo, D., 2022. 10 m crop type mapping using Sentinel-2 reflectance and 30 m cropland data layer product. International Journal of Applied Earth Observation and Geoinformation 107, 102692.
- Waha, K., Dietrich, J.P., Portmann, F.T., Siebert, S., Thornton, P.K., Bondeau, A., Herrero, M., 2020. Multiple cropping systems of the world and the potential for increasing cropping intensity. Global Environmental Change 64, 102131.
- Wang, J., Zhang, Z., Liu, Y., 2018. Spatial shifts in grain production increases in China and implications for food security. Land Use Policy 74, 204–213.
- Wu, W., Yu, Q., You, L., Chen, K., Tang, H., Liu, J., 2018. Global cropping intensity gaps: Increasing food production without cropland expansion. Land Use Policy 76, 515–525.
- Xiang, M., Yu, Q., Wu, W., 2019. From multiple cropping index to multiple cropping frequency: Observing cropland use intensity at a finer scale. Ecological Indicators 101, 892–903.
- Yan, H.M., Xiao, X.M., Huang, H.Q., Liu, J.Y., Chen, J.Q., Bai, X.H., 2014. Multiple cropping intensity in China derived from agro-meteorological observations and MODIS data. Chinese Geographical Science 24, 205–219.
- Yan, H.M., Liu, F., Qin, Y., Doughty, R., Xiao, X., 2019. Tracking the spatio-temporal change of cropping intensity in China during 2000–2015. Environmental Research Letters 14, 035008.
- Yan, L., Roy, D., Li, Z., Zhang, H., Huang, H., 2018. Sentinel-2A multi-temporal misregistration characterization and an orbit-based sub-pixel registration methodology. Remote Sensing of Environment 215, 495–506.
- Yu, L., Shi, Y., Gong, P., 2015. Land cover mapping and data availability in critical terrestrial ecoregions: a global perspective with Landsat thematic mapper and enhanced thematic mapper plus data. Biological Conservation 190, 34–42.
- Zhai, P., Li, S., He, Z., Deng, Y., Hu, Y., 2021. Collaborative Mapping Rice Planting Areas Using Multisource Remote Sensing Data, 2021 IEEE International Geoscience and Remote Sensing Symposium IGARSS, pp. 5969-5972.
- Zhang, X., 2015. Reconstruction of a complete global time series of daily vegetation index trajectory from long-term AVHRR data. Remote Sensing of Environment 156, 457–472.
- Zhang, Z., Wen, Q., Liu, F., Zhao, X., Liu, B., Xu, J., Yi, L., Hu, S., Wang, X., Zuo, L., 2016. Urban expansion in China and its effect on cultivated land before and after initiating "Reform and Open Policy". Science China Earth Sciences 59, 1930–1945.
- Zhang, M., Wu, B., Zeng, H., He, G., Liu, C., Nabil, M., Tian, F., Bofana, J., Wang, Z., Yan, N., 2021a. GCI30: Global Cropping Intensity at 30m resolution. Harvard Dataverse

Zhang, M., Wu, B., Zeng, H., He, G., Liu, C., Tao, S., Zhang, Q., Nabil, M., Tian, F., Bofana, J., 2021b. GCI30: a global dataset of 30 m cropping intensity using multisource remote sensing imagery. Earth System Science Data 13, 4799–4817.
Zhu, Z., Wang, S.X., Woodcock, C.E., 2015. Improvement and expansion of the Fmask algorithm: Cloud, cloud shadow, and snow detection for Landsats 4–7, 8, and

Sentinel 2 images. Remote Sensing of Environment 159, 269–277.

Zuo, L.J., Xiao, W., Fang, L., Ling, Y., 2013. Spatial exploration of multiple cropping efficiency in China based on time series remote sensing data and econometric model. Journal of Integrative Agriculture 12, 903–913.